Effect of annealing temperature on optical properties, microstructure and surface morphology of manganese dioxide layers

T. NAMDARI[1,*], B. ASTINCHAP[2], R. MORADIAN[3]
[1]*Department of Physics, Malek Ashtar University of Technology, 8315713115, Shahinshahr, Iran*
[2]*Research Center for Nanotechnology, University of Kurdistan, 6617715175, Sanandaj, Iran*
[3]*Physics Department, Faculty of Science, Razi University, 6714414971, Kermanshah, Iran*

In an effortlessly way, layers of manganese dioxide (MnO_2) prepared at room temperature by chemical bath deposition. The thermal treatment were investigated to obtain the best control over microstructure and optical properties of manganese oxides. Determinations show that the layers structure is σ-MnO_2 at room temperature after annealing transformed to Ramsdellite, Pyrolusite, and Manganite structures. From the transmittance spectra of the layers, the optical band gap obtained about 3.75 eV for the as-deposited layer, while different band gap after the thermal treatment depending on the annealing temperature. The results show annealing temperature affects optical factors similar to extinction coefficient, refractive index, and dielectric constant. Hope these finding will be useful in the future development of environmental friendly manganese oxide-based optical layers systems.

(Received September 20, 2022; accepted April 7, 2023)

Keywords: Manganese dioxide, Layers, Band gap, Optical properties

1. Introduction

Over the past few years, with the advancement of nanotechnology, thin films (two-dimensional nanostructures) have attracted a considerable value research. The physical properties of the thin films are generally different from the bulk material. They can be changed depending on the method and conditions of deposition and the structure of the thin films. Deposition rate, annealing temperature and time, substrate temperature, vacuum, substrate structure, and its alignment with the layer are some factors that affect the thin layer quality [1-8]. Manganese oxide is one of the significant materials in the film field owing to its non-toxicity, environmentally friendly, and high transparency [2, 3]. Manganese oxides have different structures; the most stable structures of these compounds are MnO, MnO_2, Mn_2O_3, and Mn_3O_4. Among its various compounds' MnO_2 has a simplex structure that is more permanent at room temperature than other manganese oxides. MnO_2 has 3 electrons in its 3d shell, which can display its antiferromagnetic behavior. Different methods, including sol-gel, chemical bath deposition, dip coating, spin coating, co-precipitation, hydrothermal, CVD, thermal evaporation, e-beam, and sputtering, synthesize manganese oxide thin films [9-16]. The chemical bath deposition (CBD) method is one of the simplest methods that can be used to prepare Manganese oxide thin film. The ability to employ different shapes and large-area substrates, easy control of deposition conditions, and continuous deposition are the advantages of the CBD method.

Fau et al. [15] reported that manganese oxide deposited by the sputtering method had an amorphous structure even up to 450 °C annealings. The other investigation showed the effects of different factors like evaporation rate, substrate temperature, and work pressure on optical and electrical properties of manganese oxide layers were investigated and prepared using CVD [17]. Yan et al. reported that prepared 3D porous α-MnO_2 film by a simple, low cost, safe and practical room temperature CBD had a maximum specific capacitance of 500.5 Fg^{-1} at a scan rate of 10 mVs^{-1} and exhibited the high rate capability [18]. The magnetic properties of deposited β-MnO_2 thin layers prepared using plasma-assisted molecular beam epitaxy have been studied by X. J. Xing et al. [19]. Also, the usage of manganese oxide in water treatment has been investigated, so some experimental researchers utilized manganese oxide nanowires to delete Arsenic and chromium ions from industrial wastewater [20]. In another paper, reduced graphene oxide plates and manganese oxide nanoparticles were used for the powerful immobility of flavin adenine dinucleotide (FAD) as a highly sensitive persulfate sensor [21]. Cestaro et al. investigated manganese oxides nano structures synthesized by potentiostatic electrodeposition from a de-aerated manganese acetate and sodium sulfate electrolytic bath, followed by annealing for electrochemical devices. They investigated electrodeposition parameters (including applied potential, precursor concentration, pH, temperature) and the thermal treatment conditions to obtain the best control over microstructure and stoichiometry of manganese oxides [22]. Our previous work investigated the concentration effect on optical

properties, fractal, and morphology of manganese oxide films [23]. In this study, manganese oxide layers are synthesized by chemical bath deposition procedure, and the efficacy of annealing temperature on morphology, structural, and optical properties are studied to obtain the best control over microstructure and optical properties of manganese oxides.

2. Experimental

Glass substrates were cut to the same size as 1 × 2.5 cm. Then, washed twice ultrasonically with acetone and distilled water. The deposition solution of $KMnO_4$ (purchased from Merck) in distilled water with 0.00443 mol/L was prepared in ambient conditions (the pH of solution is 7). A chemical bath deposition procedure is used to prepare MnO_2 layers. The substrates were appended horizontally in beakers containing 40 ml prepared $KMnO_4$ solution, and then 14 ml ethanol (Merck > 98%) was added rapidly to as-prepared solutions and maintained for 72 hours. The chemical reaction is done in a solution on the glass substrates as follows:

$$4KMnO_4+C_2H_5OH \Longrightarrow 4MnO_2+4KOH+H_2O+2CO_2 \quad (1)$$

Deposited layers on glass substrates were cleaned with distilled water three times to remove residual salt and let them dry in air at room temperature, as has been done in our previous work [23]. To study the effects of annealing temperature on prepared manganese oxide films, the layers were annealed at different temperatures of 100 °C, 200 °C, and 300 °C for one hour in a normal atmosphere.

The prepared films were characterized by scanning electron microscopy (SEM), differential scanning calorimetry (DSC), atomic force microscopic (AFM), UV-Vis spectrophotometer to study optical properties, and X-ray diffraction (XRD) to identify the structure and crystalline phase.

3. Results

Synchronous thermal analysis (DSC) for as-deposited MnO_2 was performed in the range of room temperature up to 600 °C (Fig. 1). As seen in the DSC curve, an endothermic peak is observed at the temperature of 100 °C, which corresponds to the loss of surface absorbed water. The region below 350 ˚C has detected three exothermic peaks, corresponding to a phase change or a chemical transformation. Minor peaks may be attributed to the bond formation, breakage of the bond, or a total change in structure; for more investigation, XRD at these temperatures (100, 200, 300 ˚C) was compared.

X-ray diffraction (XRD) analysis of the layer at room temperature was demonstrated in Fig. 2. As seen, the structure of the prepared samples is σ-MnO_2 according to diffraction patterns of the σ-MnO_2 standard sample with PDF number 00-018-0802. This structure, as mentioned in the introduction, includes additional ions such as potassium among the plate joints of the MnO_6 chains. Unlike Cestaro's as-electrodeposited layers [22], which were amorphous, our produced as-deposited layers have crystalline structure at room temperature.

Fig. 3 illustrates XRD patterns for the layers annealed at 100, 200, and 300 °C temperatures. It is seen that the layer that annealed at 100 °C is the contribution by different structures of Ramsdellite (00-005-0331), Pyrolusite (00-003-0551), and Manganite (00-008-0099). Three peaks are observed in the sample annealed at 200 °C temperature. The peak of the Manganite structure observed in the annealed layer at 100 °C turns into a Pyrolusite structure.

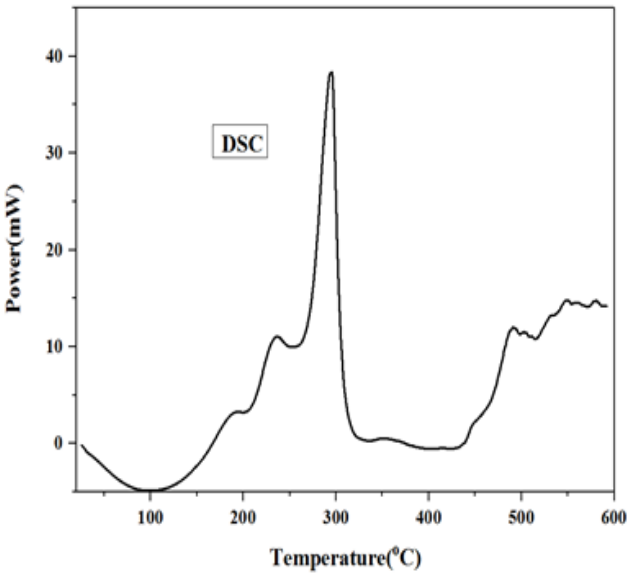

Fig. 1. DSC spectrum of the as deposited layer

Also, in the XRD pattern of the layer that annealed at 300 °C seen, several peaks of Pyrolusite and just a peak of Ramsdellite structure. Therefore, it concluded that by increasing the annealing temperature, the Ramsdellite structure appears more. The average crystallite size is obtained by the Debye-Sherrer equation:

$$D = 0.9 * \lambda/\beta \cos\theta_\beta \quad (2)$$

where D, θ_β, and β are the crystallite size, half of the diffraction angle, and the broadening, respectively. The calculated crystal size for as-deposited 100, 200, and 300 °C layers are 17, 30.5, 35.7, and 39.3 nm in sequence. According to this calculated data, it is seen that with increasing annealing temperature, the average crystalline size has increased. In general, it can be concluded that the thermal convection in the DSC at 100 °C is due to the structural transformation of a σ-MnO_2 structure into Ramsdlite, Pyrolusite, and manganite. It is observed that the thermic peaks at temperatures of 200 °C and 300 °C are due to a change in the structure of the Pyrolusite structure, which is the purest structure of manganese dioxide. The pyrolusite structure is the purest structure of

manganese dioxide because it consists of fewer additional components (such as K+, etc.) than other structures of manganese dioxide.

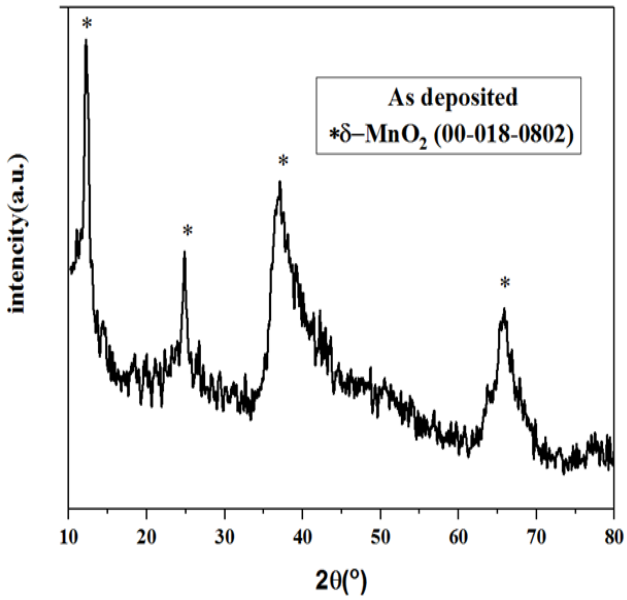

Fig. 2. X-ray diffraction pattern of as deposited sample at room temperature

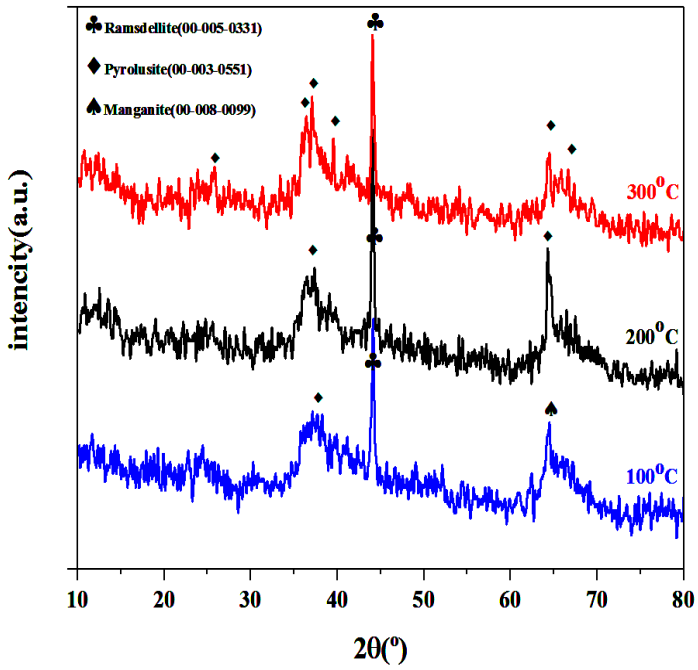

Fig. 3. Crystal structures of annealed samples at three different temperatures (color online)

SEM images of the layers are shown in Fig. 4. Growing the layer on the substrate is according to three mechanisms: a. island formation (Volmer–Weber), b. layer-by-layer (Frank-van der Merwe), and c. layer-plus-island (Stranski-Krastanov). As seen in Fig. 4(a), for the as-deposited layer, the growth of the manganese oxide layers on the glass substrate has followed the model of Volmer-Weber (island formation).

The deformation process of the islands is such that in the as-deposited layer, these islands are nanoparticles with a 67 nm average size. But, for the deposited layer annealed at 100 °C, the SEM image shows the layer surface is more similar to the third model (Stranski-Krastanov (layer-plus-island)) that the islands are nanoparticles with an average of 84 nm (Fig. 4(b)). It can be seen that by annealing the deposited layer at 200 °C, the average size of these islands has grown to 110 nm (Fig. 4(c)). By annealing at a temperature of 300 °C, the islands are composed of nanoparticles with an average size of 90 nm and needle-shaped particles with an average length of 648 nm and a mean diameter of 79 nm (Fig. 4(d)), which shows the formation of a new form of this structure with annealing

temperature. Based on this process of change in the surface of the layers due to the annealing temperature, it can be concluded that by heating the samples, nanoparticles close are continuously growing and creating larger particles with different shapes. The thickness of deposited layers is obtained by a cross-section SEM image, shown in Fig. 5. It shows that the thickness of the deposited layer is 0.34 µm.

AFM analysis was used to study further the quantitative and qualitative features of the sample surface. 3D-AFM images of the surface of the layers are depicted in Fig. 6. From this analysis, the surface roughness of the samples was obtained as follows: The surface roughness of the as-deposited layer is 8 nm, the surface roughness of annealed layer at 100 ^{o} C is 13 nm, the roughness of the layer annealed at a temperature of 200 °C is 7 nm, and the surface roughness of the layer annealed at 300 ^{o}C is 6 nm. It is observed that the roughness of the surface is annealing temperature-dependent and varies with temperature. So, the surface roughness of the annealing sample at 100 °C is increased compared to the the surface of the samples decreased, which indicates that the growth was in line with the surface which is in good agreement with the SEM images of the sample surface. The UV-Vis spectrum for the layers was recorded in 300-1000 nm, as shown in Fig. 7. It is observed that annealing changes the absorption spectra and leads to more transparency. Samples that are annealed at 100 and 200 ˚C possess less amount absorption or higher transmittance spectra which may be a result of higher oxygen penetration during heat treatment. Although the higher absorption of the annealed sample at 300 ˚C may be attributed to the growth of film crystalline thickness, as concluded from XRD results.

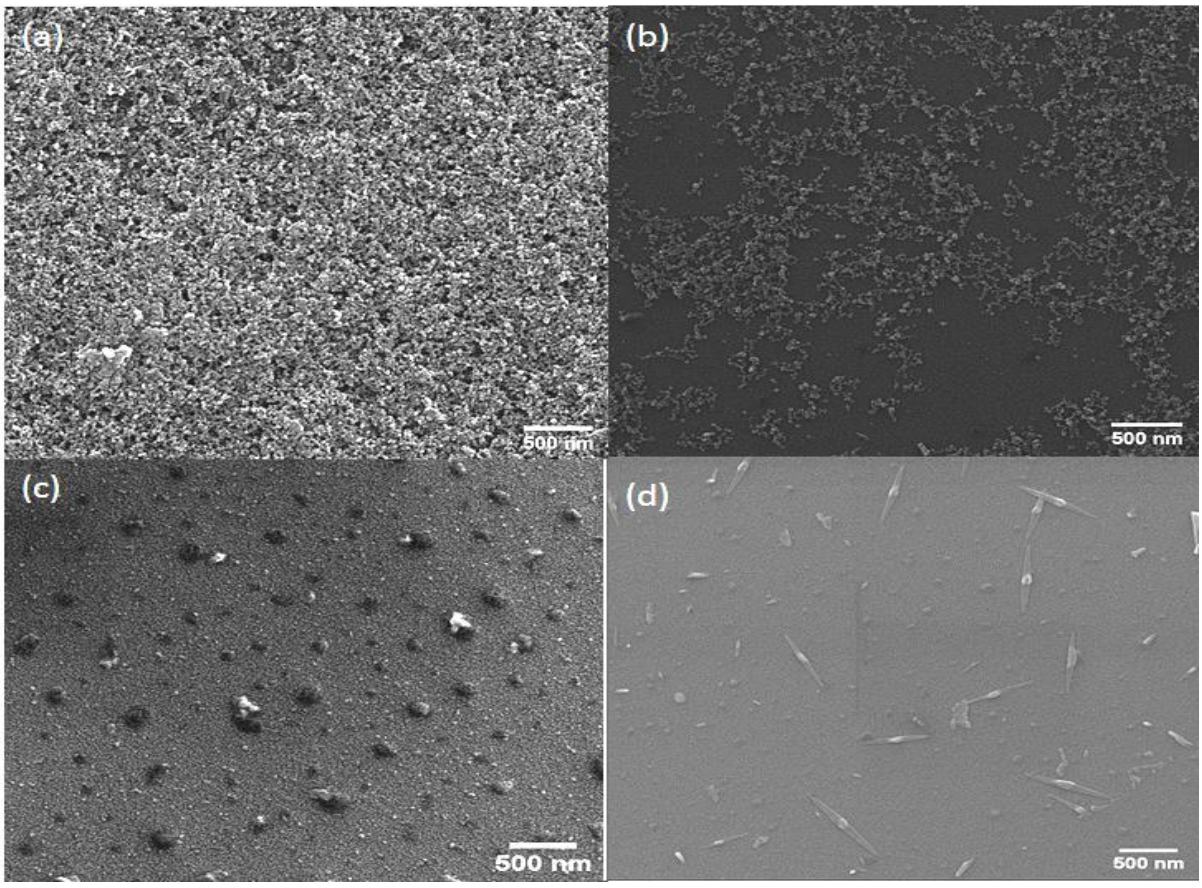

Fig. 4. SEM image of the surface layer of (a) as deposited, (b) the annealed layer at 100 ^{o}C, (c) 200 ^{o}C, (d) 300 ^{o}C

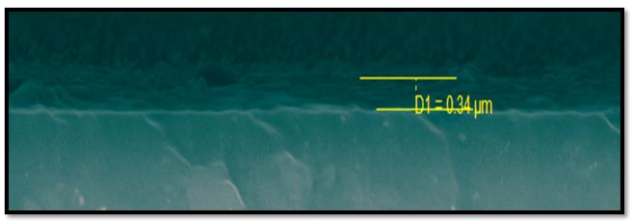

Fig. 5. Obtained thickness of deposited layers by cross section SEM image (color online)

The optical band gap of samples is obtained from the optical curve in terms of wavelength by the following equation [26]:

$$\alpha h\nu = A\left(h\nu - E_{opt}\right)^{s} \quad (3)$$

where α is the absorption coefficient, hν is the photon energy, A is the constant, and s defines transition type,

which for indirect transition and the direct transition is s=2 and 1/2, respectively. α is calculated by [27]:

$$\alpha = \frac{\ln(\frac{1}{T})}{d} \quad (4)$$

The curve of $(\alpha h\nu)^{0.5}$ in terms of hν is illustrated in Fig. 8. Extrapolation of the linear portion of the curve to $(\alpha h\nu)^{0.5} = 0$ gives the band gap values. It is obtained that the best fitting of the experimental data to Eq. (3) is the indirect allowed transition, which is shown in Fig. 8.

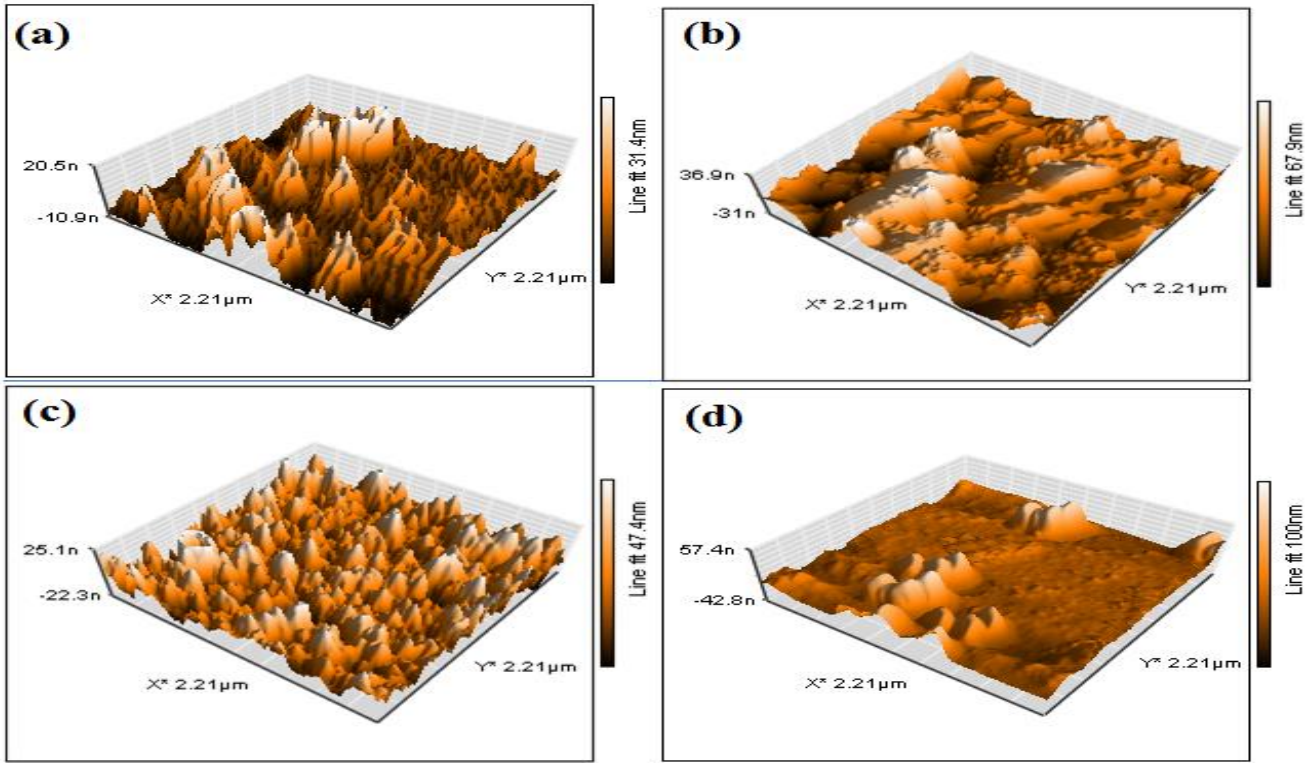

Fig. 6. Atomic Force Microscopy image of (a) the as-deposited surface, the sample annealed at (b) 100 °C, (c) 200 °C, (d) 300 °C

The band gap energy values of as-deposited and the annealed films are demonstrated in Table 1. Changing gap energy by annealing can be ascribed to alterations of the disorder and lattice defects system present in the materials [17]. Emerging Pyrolusite phase structure may cause the larger band gap energy; refer to XRD results. Refractive index (n), real and imaginary parts of the optoelectric constant (the complex dielectric constant is a crucial opto-electric constant that shows essential inherent properties of materials), can be calculated as following and are shown in Fig. 9:

$$A + T + R = 1 \quad (5)$$

$$k = \alpha\lambda/4\pi \quad (6)$$

$$n = \frac{1+R}{1-R} + \sqrt{\left(\frac{4R}{(1-R)^2}\right) - k^2} \quad (7)$$

$$\varepsilon_r = n^2 - k^2 \quad (8)$$

$$\varepsilon_i = 2nk \quad (9)$$

Extinction coefficient (*k)* for the samples; *k* changes by annealing process steps are illustrated (Fig. 9 (a)). It is indicated that the extinction coefficient decreases slightly, which is related to the oxide layer. Refractive indices of the as-deposited and annealed samples are shown in Fig. 9 (b); more oxidized layers have a lower refractive index [26]. This may be attributed to more porous layers and an increase in scattering centers originating from surface roughness and vacancies [24]. It is clear that the Pyrolusite phase is as denser as Ramsdellite, and the decrease in refractive index is consistence with XRD results. The loss factor is equal to the ratio of the imaginary part to the real part [26,27]. The dependence of ε_r and ε_i in terms of photon energy is illustrated in Fig. 9 (c) and (d). The real part of the dielectric constant represents values larger than its imaginary part at the investigated photon energy.

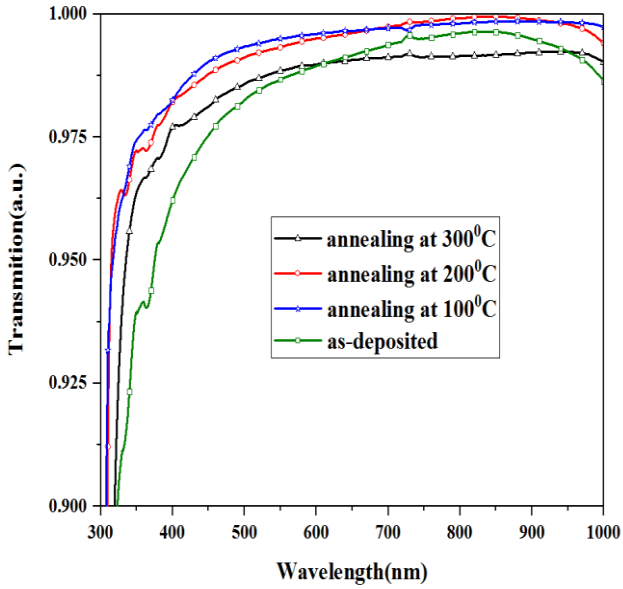

Fig. 7. Transmittance, T(λ), spectra for as-deposited and annealed layers at 100 ºC, 200 ºC and 300 ºC (color online)

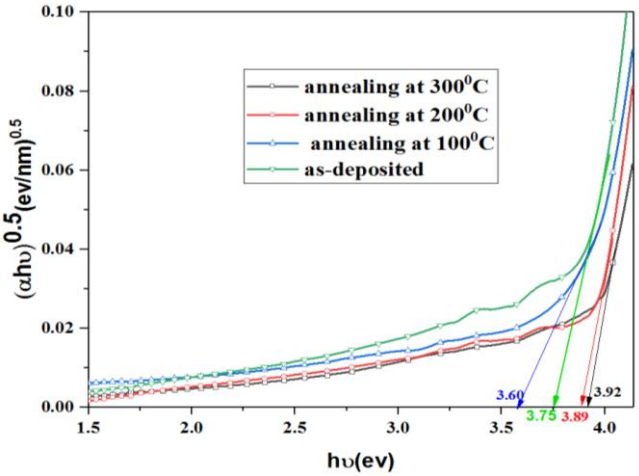

Fig. 8. Plot of $(\alpha h\nu)^{0.5}$ vs. (hν) for as-deposited and annealing films (color online)

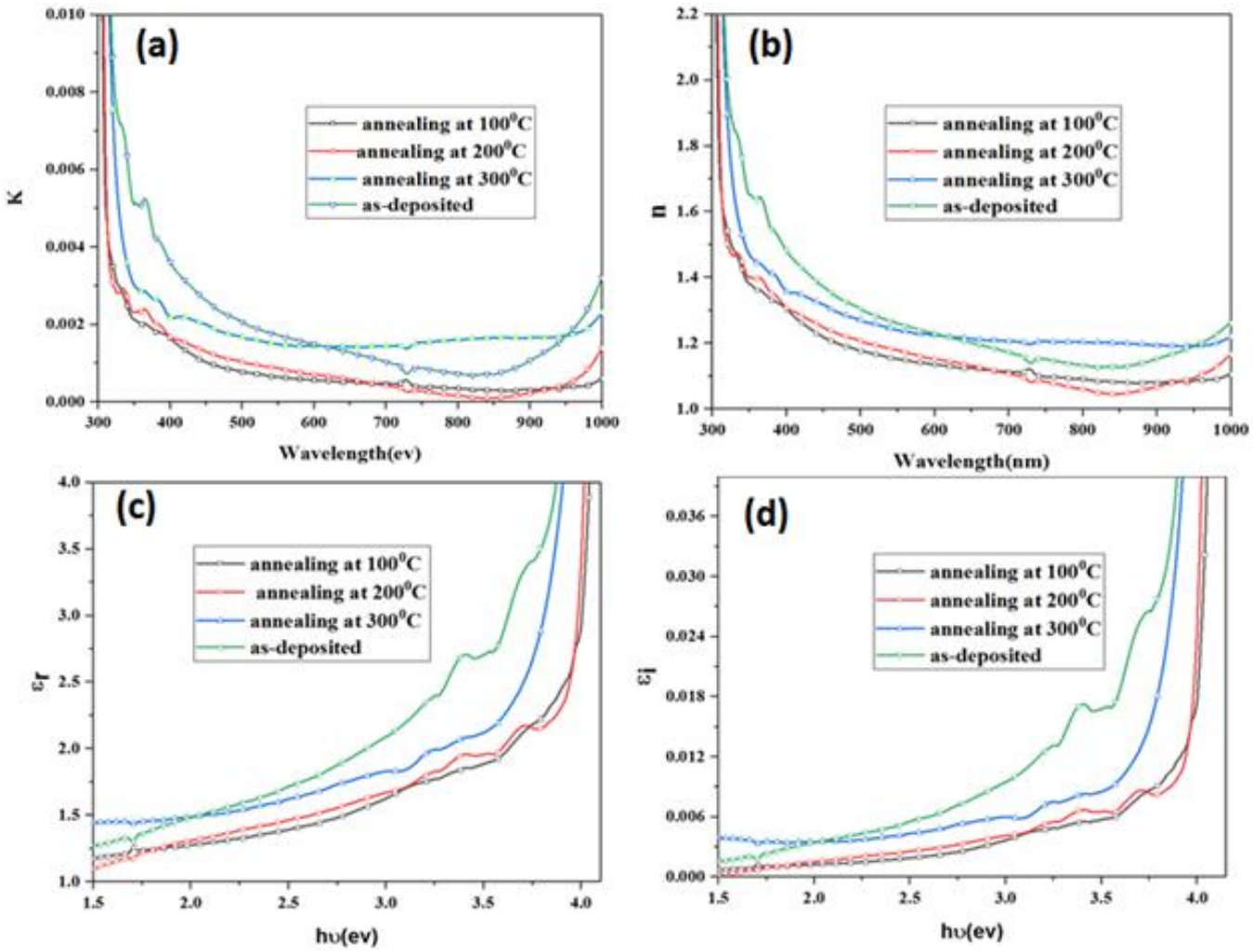

Fig. 9. (a) Refractive index, (b) coefficient index in term of wavelength, (c) real part, and (d) imaginary part of the dielectric constant in term of photon energy for different layers (color online)

The alteration of the dielectric constant in terms of the photon energy explains that different interactions between electrons and photons were produced in the layers in this area of energy. The appearance of the peaks in the dielectric curve due to these interactions [17].

Table 1. Summary of information on the energy band gap for annealing layers at various temperatures

Annealing temperature	**Band gap energy (eV)**
As deposited	3.75
100 °C	3.60
200 °C	3.89
300 °C	3.92

4. Conclusions

With the synthesis of MnO_2 films under the same conditions, we investigated the efficacy of various annealing temperatures on morphological, optical, and structural properties of the surface of the layers. With an increase in the temperature of annealing, the size of the islands was increased on the edges so that they were observed in the form of nanoparticles for the annealed sample at 300 ^oC. It was obtained from optical studies that the optical band gap, extinction coefficient, refractive index, and imaginary and real part dielectric constant of layers changed with increasing annealing temperature, confirming the growth of nano-crystals. The results show that the optical band gap increase with the decrease in annealing temperature to 100 ºC (from 3.76 to 3.60 eV) and then increases at 300 ºC to 3.92 eV. As we have seen, with the change of annealing temperature, which initially had a non-site structure, the structure changed and gradually moved into the structure of Pyrolusite, which is a pure structure of MnO_2.

References

[1] K. Ulutas, D. Deger, Y. Skarlatos, Phys. Stat. Sol. **203**(10), 2432 (2006).
[2] W. Xia, D. Wang, X. Lou, J. Phys. Chem. **114**(3), 1694 (2010).
[3] Z. Lio, Y. Xing, C. Chen, L. Zhao, L. S. Suib, Chem. Mater. **20**(8), 2069 (2008).
[4] A. Salimi, S. Mansouri Majd, B. Astinchap, Biosens. Bioelectron. **92**(8), 733 (2017).
[5] M. Molamohammadi, A. Arman, A. Achour, B. Astinchap, A. Ahmadpourian, A. Boochani, S. Naderi, A. Ahmadpourian, J. Mater. Sci.: Mater. Electron. **26**(8), 5964 (2015).
[6] B. Astinchap, Optik **178** (8), 231 (2019).
[7] A. Salimi, S. Mansouri Majd, B. Astinchap, Sens. Actuators B Chem. **266**(8), 178 (2018).
[8] S. Abdolghaderi, B. Astinchap, J. Mater. Sci.: Mater. Electron. **27**(7), 6713 (2016).
[9] S. C. Pang, B. H. Wee, S. F. Chin, Int. J. Electrochem. **2011**(8), 397685 (2011).
[10] M. Toupin, T. Brousse, D. Belanger, Chem. Mater. **16**(16), 3184 (2004).
[11] L. Zhang, L. Kang, H. Lv, Z. Su, J. Mater. Res. **23**(3), 780 (2008).
[12] J. W. Long, L. R. Qadir, R. M. Stroud, D. R. Rolison, J. Phys. Chem. B. **105**(37), 8712 (2001).
[13] M. F. Al-Kuhaili, J. Vac. Sci. Technol. A. **24**(5), 1746 (2006).
[14] K. Neishi, S. Aki, K. Matsumoto, H. Sato, H. Itoh, S. Hosaka, J. Koike, Appl. Phys. Lett. **93**(3), 032106 (2008).
[15] S. Kumar, R. B. Choudhary, Mater. Sci. Semicond. **139**(8), 106322 (2022).
[16] A. K. M. F. U. Islam, R. Islam, K. A. Khan, Renew. Energ. **30**(15), 2289 (2005).
[17] A. R. Merritt, R. Rajagopalan, J. D. Carter, Thin Solid Films **556**(4), 28 (2014).
[18] D. Yan, Z. Guo, G. Zhu, H. Yang, R. Wei, H. Xu, A. Yu, Mater. Lett. **82**(8), 156 (2012).
[19] A. K. M. F. U. Islam, R. Islam, K. A. Khan, J. Mater. Sci.: Mater. Electron. **16**(4), 203 (2005).
[20] S. Panimalar, M. Chandrasekar, S. Logambal, R. Uthrakumar, C. Inmozhi, Mater. Today: Proc. **56**(3), 3394 (2022).
[21] A. Salimi, S. Mansouri Majd, B. Astinchap, Electroanalysis **28**(3), 493 (2015).
[22] R. Cestaro, P. Schweizer, L. Philippe, X. Maeder, A. Serra, Appl. Surf. Sci. **580**(3), 152289 (2022).
[23] B. Astinchap, R. Moradian, T. Namdari, S. Jurečka, Ş. Ţălu, Opt. Quantum Electron. **51**(6), 1 (2019).
[24] M. K. Hamad, M. Sayyed, M. Mhareb, M. Sadeq, N. Dwaikat, M. Almessiere, Kh. A. Ziq, Opt. Mater. **127**(8), 112350 (2022).
[25] D. Pjević, M. Obradović, T. Marinković, A. Grce, M. Milosavljević, R. Grieseler T. Kups, M. Wilke, P. Schaaf, Phys. B: Condens. Matter. **463**(8), 20 (2015).
[26] B. Astinchap, R. Moradian, K. Gholami, Mater. Sci. Semicond. Process. **63**(8), 169 (2017).
[27] I. Manouchehri, K. Gholami, B. Astinchap, R. Mordian, D. Mehrparvar, Optik **127**(13), 5383 (2016).

*Corresponding author: tahereh.namdari@yahoo.com